Spatiotemporal Analysis of the Potential Impact of the Masinloc Power Plant on the Thermal Pollution in Oyon Bay, Zambales, and its Correlation to the Seagrass Cover

Leonard Gelo E. Galinato[1], Alessandra M. Tolentino[1], Ayin M. Tamondong[1,2], Jommer M. Medina[1,2], Severino G. Salmo III[3]

[1]Department of Geodetic Engineering, University of the Philippines Diliman, Quezon City, Philippines - {legalinato, amtolentino6, amtamondong, jmmedina}@up.edu.ph
[2]Training Center for Applied Geodesy and Photogrammetry, University of the Philippines Diliman, Quezon City, Philippines
[3]Institute of Biology, University of the Philippines Diliman, Quezon City, Philippines - sgsalmo@up.edu.ph

Keywords: sea surface temperature, space-time cube, seagrass, stress, recovery, time lag, single-channel algorithm

Abstract

The proximity of power plants to protected seascapes presents a significant environmental concern, yet research on thermal pollution and its effects on marine ecosystems in the Philippines remains limited. This study examined the relationship of thermal pollution from the Masinloc Power Plant on the marine ecosystem of Oyon Bay, Zambales, focusing on seagrass ecosystems. Remotely sensed sea surface temperature (SST) data from Landsat satellites (5, 7, and 8) were used to track SST changes from the pre-operation period (1993-1998) to the operational period (1999-2023). Time series decomposition of SST data indicates a gradual increase in temperature, with emerging hotspots analysis identifying localized thermal pollution near the plant's outfall. A time-lagged correlation analysis revealed a moderate negative relationship (R = -0.47) between increased SST and seagrass percent cover, with a delayed response of approximately seven months. Seagrass cover significantly decreased after the plant started operating but showed partial recovery over time. These findings highlight the adverse effects of thermal pollution on seagrass ecosystems, emphasizing the need for effective management strategies to mitigate such impacts. This research contributes to the limited understanding of thermal pollution in marine protected areas, offering valuable insights for environmental monitoring and policy development.

1. Introduction

1.1 Background of the Study

Despite the global push for renewable energy, the Philippines remains heavily reliant on coal-fired power plants, which accounted for 63.7% of the country's gross power generation in 2023 (Department of Energy, 2024). One major contributor is the Masinloc Power Plant located in Barangay Bani, Masinloc, Zambales. Initially a two-unit 600 MW facility when it began operations in 1998, it has since expanded to 1,019 MW. Like other coal-fired plants, it requires large volumes of water for cooling—often drawn from and discharged back into nearby bodies of water. This process causes thermal pollution, which poses significant threats to aquatic ecosystems (Mishra et al., 2021).

The intake and outfall of the Masinloc Power Plant are located within the Masinloc and Oyon Bay Protected Landscape and Seascape (MOBPLS), or more commonly known as Oyon Bay. This is an area rich in seagrass meadows, coral reefs, mangrove forests, and fisheries (Paz-Alberto et al., 2015). These ecosystems, especially seagrasses, are sensitive to temperature changes. A 5°C increase can disrupt photosynthesis and respiration in seagrasses, while prolonged exposure to heat can cause physiological stress and sediment hypoxia (Jiang et al., 2022). Although tropical seagrasses can tolerate 23°C–32°C, extreme and sustained heat can reduce biomass and weaken carbon storage capacity (Macreadie & Hardy, 2018). In fact, Reyes et al. (2021) observed degraded seagrass meadows near the plant, with low biomass and high organic carbon linked to ash and warm wastewater.

Given this context, tools like the space-time cube can be used to analyze spatiotemporal patterns of thermal pollution. This 3D data visualization method represents spatial dimensions on the horizontal plane and time on the vertical axis, helping to detect trends, clusters, and changes across time and space (Bach et al., 2014).

1.2 Research Objectives

The study generally aims to investigate the potential thermal pollution caused by the Masinloc Power Plant in Oyon Bay and its effect on the marine ecosystem of the area by using remote sensing techniques. Specifically, it aims to: (1) Determine the occurrence of thermal pollution in Oyon Bay through analysis of historical SST data pre-operation (1993-1998) to present operation (1999-2023) of the Masinloc Power Plant; (2) Investigate the potential contribution of the Masinloc Power Plant to the thermal pollution in the coastal region by determining the spatiotemporal clustering using a space-time cube and hotspot category through emerging hotspots analysis, and (3) Determine the correlation between the change in temperature and the seagrass cover in the study area through a lagged correlation analysis.

1.3 Significance of the Study

Given its marine-protected status, monitoring water quality (particularly temperature changes) is crucial to protecting the bay from adverse effects of thermal pollution. By utilizing Landsat satellite data, which provides high spatial resolution, long-term, and large-scale sea surface temperature (SST) data, this study addresses a gap in Philippine research where few studies have focused on remote-sensed SST data to track thermal pollution over time. The study of Yavari and Qaderi (2018) on the determination of thermal pollution of water resources caused by the Neka power plant in Iran used Landsat 8 satellite imagery in extracting the water temperature around the outlet of the power plant through the thermal infrared sensors (TIRS), which has two thermal bands – Bands 10 and 11. Furthermore, data from this research can help the municipal government craft informed policies and regulations

https://doi.org/10.5194/isprs-annals-X-5-W4-2025-261-2026 | © Author(s) 2026. CC BY 4.0 License.

to mitigate the impact of thermal pollution, preserve the bay's ecology, and support sustainable resource use. This research aligns with the United Nations Sustainable Development Goal (SDG) 14, particularly targeting 14.1, which focuses on reducing marine pollution, and 14.2, which emphasizes sustainably managing and protecting marine and coastal ecosystems.

1.4 Scope and Limitation

This study focuses on assessing thermal pollution through SST data in the MOBPLS and specifically examines the potential impact of the Masinloc Power Plant on the bay's seagrass ecosystems. The temporal scope included both a pre-operational period (1993–1998) and an operational period (1999–2023), with SST data sourced from Landsat 5, 7, and 8 satellites. Data collection was dependent on the availability and clarity of satellite imagery, which was constrained by cloud cover and the revisit period of the mentioned satellite systems. Moreover, seagrass cover was estimated without differentiating between species, which limited the analysis of species-specific spectral variability and thermal tolerance. Also, this study did not take into account global climate models. The effects brought by climate change were beyond the scope of the analysis in this study.

2. Methodology

2.1 Study Area

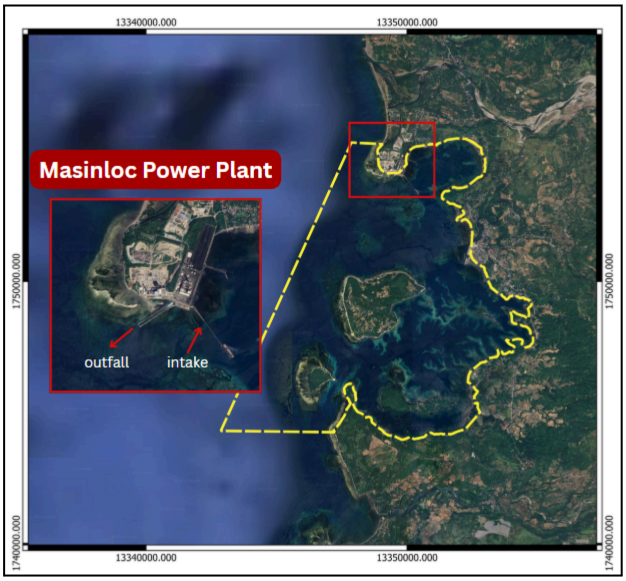

Figure 1. The study area

The Masinloc-Oyon Bay was designated as a marine protected area (MPA) under Republic Act No. 7586, also known as the National Integrated Protected Areas System Act on August 18, 1993. This declaration ensured the conservation of its unique marine biodiversity, including mangroves, seagrass, and coral reefs, which are crucial to the local ecosystem (Mayuga, 2021). The area, officially known as the Masinloc-Oyon Bay Protected Landscape and Seascape (MOBPLS), became the first marine protected area (MPA) in Central Luzon. It spans 7,558 hectares and has become a key site for environmental preservation in the region. In Figure 1, the location of the Masinloc Power Plant relative to MOBPLS is highlighted. Also shown in the figure are the locations of the intake where the cooling water is sourced from and the outfall where the heated byproducts are dumped.

2.2 General Flowchart

The methodology of this study was structured into three main phases as shown in Figure 2. The first phase involved the extraction of SST data and the identification of thermal hotspots. The second phase focused on the estimation of seagrass percent cover. Both phases were preceded by essential preprocessing steps and included appropriate validation procedures to ensure data quality and accuracy. The outputs generated from these initial phases served as the primary inputs for the final phase, which entailed a time-lag correlation analysis between SST and seagrass cover.

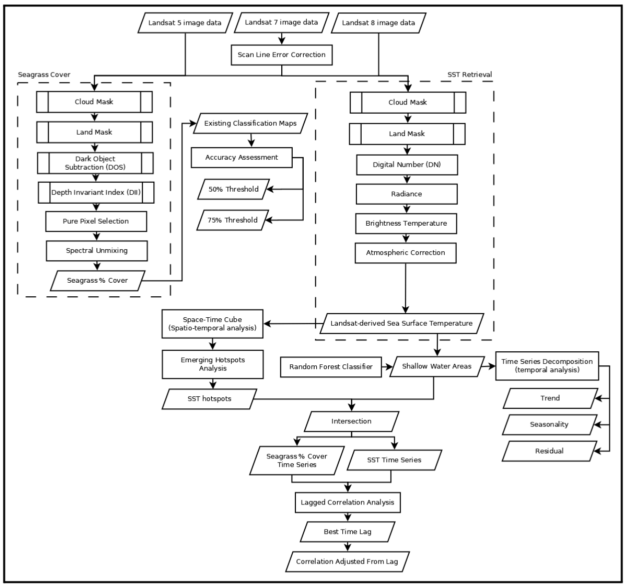

Figure 2. Flowchart of the study

2.3 Datasets Used

Table 1 shows the image data that were used in this study. The same datasets were used for the retrieval of the SST and the seagrass percent cover for uniformity. Since the data needed in this study covers the period before and during the operation of the Masinloc Power Plant, Landsat 5, 7, and 8 imagery were used to cater this temporal need.

Data	Band Used (for SST)	Resolution	Source
1993-2000, 2004-2010 Landsat 5 TM Collection 2 Tier 1 Raw Scenes (Level 1)	6 (Thermal Infrared)	30 m	USGS
2001-2003, 2011-2013 Landsat 7 Collection 2 Tier 1 Raw Scenes (Level 1)	6 (Thermal Infrared)	30 m	USGS
2014-2023 Landsat 8 Collection 2 Tier	10 (Thermal	30 m	USGS

https://doi.org/10.5194/isprs-annals-X-5-W4-2025-261-2026

1 Raw Scenes (Level 1)	Infrared)		

Table 1. Image Datasets for SST and seagrass cover retrieval

2.4 Preprocessing

2.4.1 Scan Line Correction: To correct the scan line errors, a custom function was applied in Google Earth Engine (GEE). This approach works by identifying the missing pixels in the image and estimating their values through spatial interpolation. Specifically, it calculated the average of surrounding valid pixels using a focal mean technique which smooths over the gaps while preserving the general characteristics of the image. The interpolated values were then merged with the original data to create a corrected image.

2.4.2 Cloud Mask: The presence of clouds and its shadows within the dataset obscured the features below it, preventing the satellite from detecting the said features. Hence, using the QA_Pixel band of the Landsat imagery, clouds, shadows, and cirrus clouds were detected. Then, a binary mask was created to mask out clouds and cloud shadows where pixels affected by these said features became null.

2.4.3 Land Mask: The water body was separated from the land through Land Masking by creating a binary mask using the JRC Global Surface Water dataset which was run on GEE. This ~~said~~ dataset was derived from Landsat imagery hence, it has a spatial resolution of 30 meters, and covered the temporal need of the study.

2.4.4 Water Column Correction using Depth Invariant Index (DII): To minimize depth-related reflectance variation, the Depth Invariant Index (DII) was computed in GEE using surface reflectance imagery. Selected band pairs were used, and three sand pixels at varying depths were manually identified to estimate the slope (k), representing the ratio of attenuation coefficients. These values were then applied to normalize reflectance using the DII formula, enhancing the accuracy of seagrass classification in optically shallow waters.

2.4.5 Dark Object Subtraction for Atmospheric Correction: To improve spectral clarity and classification accuracy, atmospheric haze was corrected in GEE using dark object subtraction. Deep water pixels served as reference dark objects, with the 1st percentile reflectance values from the visible bands subtracted across the image to reduce atmospheric scattering.

2.4.6 Shallow Water Delineation: To ensure that SST values reflected conditions relevant to seagrass ecosystems in Oyon Bay, the analysis focused on shallow coastal areas, where dominant seagrass species typically occur (Paz-Alberto et al., 2015). These zones were delineated through supervised classification using recent Landsat 8 imagery, selected over older sensors like Landsat 5 to better capture current shoreline configurations—especially important in areas like Masinloc where coastal development may have altered the coastline.

2.5 SST Retrieval

Since Landsat 5 and 7 each have only one thermal band (band 6), the single-channel (SC) algorithm was utilized. This algorithm, based on the Radiative Transfer Model, is commonly employed for retrieving surface temperature from Landsat series data (Wang et al., 2018). While Landsat 8 includes an additional thermal band (band 11), calibration issues make it unsuitable for multi-band atmospheric corrections, such as the split-window algorithm. Radiance values were first extracted from the thermal band of the satellite images using Equation (1).

$$L = M \times DN + A \qquad (1)$$

where L: Radiance
M: Radiance multiplicative scaling factor (specific to satellite and band)
A: Radiance additive scaling factor (specific to satellite and band)
DN: Digital number from the thermal band

Consequently, the radiance values were used to compute the brightness temperature using Planck's Inverse Function shown in Equation (2).

$$T^{2}_{sen} = \frac{K_2}{ln(\frac{K_1}{L}+1)} \qquad (2)$$

where T^{2}_{sen}: Brightness temperature (Kelvin)
K_1, K_2: Thermal calibration constants (specific to satellite and band)
L: Radiance

Atmospheric correction was then applied in computing SST, using a coefficient matrix derived from the SAFREE atmospheric sounding database, which is specific to each Landsat platform. The coefficient matrices for the thermal band of each satellite system are shown in Table 2 (Jiménez-Muñoz et al., 2009).

Satellite	Coefficient Matrix		
Landsat 5	0.05261	0.05933	1.01123
	-0.36368	-2.20569	0.55116
	-0.07237	1.76355	-0.47457
Landsat 7	0.04597	0.06269	1.00818
	-0.32297	-2.16801	0.55698
	-0.06397	1.69324	-0.45747
Landsat 8	0.04019	0.02916	1.01523
	-0.38333	-1.50294	0.20324
	0.00918	1.36072	-0.27514

Table 2. Coefficient Matrix Used per Satellite image

$$\begin{bmatrix} \psi_1 \\ \psi_2 \\ \psi_3 \end{bmatrix} = \begin{bmatrix} c_{11} & c_{12} & c_{13} \\ c_{21} & c_{22} & c_{23} \\ c_{31} & c_{32} & c_{33} \end{bmatrix} \begin{bmatrix} w^2 \\ w \\ 1 \end{bmatrix} \qquad (3)$$

where Ψ: atmospheric functions
w: water vapor content
c: matrix coefficients

The average water vapor content of the study area during the specific time step corresponding to the satellite image was derived using data from the National Centers for Environmental Prediction (NCEP). This value was used to construct the water vapor vector, shown in Equation (3), which was then multiplied by the coefficient matrix to obtain the psi matrix. The entries of the psi matrix were used to calculate the gamma and delta values, which were subsequently used in the estimation of SST, as shown in Equation (4).

$$T_s = \gamma\left[\frac{1}{\varepsilon}\left(\psi_1 L_{sen} + \psi_2\right) + \psi_3\right] + \delta \qquad (4)$$

$$\gamma = \frac{T_{sen}^2}{b_\gamma L_{sen}} \qquad (5)$$

$$\delta = T_{sen} - \frac{T_{sen}^2}{b_\gamma} \qquad (6)$$

where ε : Surface emissivity
L_{sen} : At-sensor radiance
γ: Gamma parameter
δ: Delta parameter
b_γ: K_2 thermal constant
T_s: Sea surface temperature
T_{sen}: At-sensor brightness temperature

2.6 Time Series Decomposition

Figure 3. Delineated shallow areas

The SST time series was decomposed into three fundamental components: trend, seasonality, and residual. The decomposition used an additive model, expressed as:

$$SST(t) = T_{trend}(t) + T_{seasonal}(t) + T_{residual}(t) \qquad (7)$$

where T_{trend} = trend component of the SST time series
$T_{seasonal}$ = seasonal component of the SST time series
$T_{residual}$ = residual component of the SST time series

The area of interest was filtered such that the classified shallow waters were extracted (see Figure 3). A time series decomposition was conducted in RStudio using SST data derived from Landsat imagery. A time series object was then created with monthly frequency, starting from the earliest year and month in the dataset. To break down the SST values into interpretable components, STL decomposition was performed using the stl() function.

2.7 Spatiotemporal Analysis of SST

To identify SST hotspots, a space-time cube (STC) was created using yearly median SST composites from 1998 to 2023, which helped reduce seasonality and data gaps. The STC was built in ArcGIS Pro by stacking annual SST raster files with 30x30 m pixel resolution, setting temporal intervals to the first day of each year, and using spline interpolation to fill missing data.

Emerging Hotspots Analysis was then applied to detect spatiotemporal clusters of high SST values linked to the plant's operations. The method used the K nearest neighbors algorithm with eight spatial neighbors (surrounding pixels) and a one-year temporal step. This setup allowed precise identification of thermal plumes while minimizing overgeneralization. By focusing on changes within a one-year window, the analysis highlighted the localized thermal effects of the power plant, distinguishing them from broader climate trends.

2.8 SST Accuracy Assessment

Due to the lack of in situ sea surface temperature (SST) data, proxy validation was used to assess the SST retrieval method. Instead of directly validating SST, the study examined the correlation between satellite-derived land surface temperature (LST) and air temperature data from the nearby PAGASA station in Iba, Zambales. Maximum monthly air temperatures from 1993 to 2023 were compared to LST retrieved using the same single-channel algorithm as SST, differing only in emissivity estimation.

2.9 Seagrass Mapping

Seagrass percent cover was estimated using linear spectral unmixing in Google Earth Engine (GEE), which decomposed each pixel into fractional contributions from four endmember classes: seagrass, coral, sand, and deep water. Seagrass endmembers were identified using field data, NAMRIA, the Allen Coral Atlas, and maps from Reyes et al. (2021). Coral endmembers were selected through spatial overlays, while sand and deep water were identified through manual image interpretation. Due to limited spatial and temporal availability of ground truth data, conventional accuracy assessments such as confusion matrices were not feasible. Instead, a threshold-based classification was performed using ≥50% and ≥75% membership values to define seagrass pixels, following Hill et al. (2024). The classified maps were vectorized in GEE and exported to QGIS for spatial validation. There, the results were compared with the existing datasets by computing the area of spatial overlap as a proxy for classification accuracy.

2.10 SST and Seagrass Time-Lagged Correlation Analysis

To take into account the delayed response of seagrass towards the increase of temperature, a time-lagged correlation analysis was done. In the study of Zhang et al. (2021), "individual 1 month lag" refers to the values of the dependent variable which are lagged by a month and are affected by the values of the independent variable of the preceding month. In this case, the dependent variable was the seagrass percent cover while the independent variable was the SST. Equation (8) obtained the correlation coefficient between the said variables.

$$r_k(x, y) = \frac{\sum_{i=1}^{n-k} (x_i - \overline{x_i})(y_{i+k} - \overline{y_{i+k}})}{\sqrt{\sum_{i=1}^{n-k} (x_i - \overline{x_i}) \cdot \sum_{i=1}^{n-k} (y_{i+k} - \overline{y_{i+k}})}} \tag{8}$$

where x_i = time series of the seagrass percent cover
y_i = time series of the sea surface temperature
n = length of time series
k = time lag (in months)

Shallow water areas were intersected with regions identified as intensifying and persistent SST hot spots, reducing the area of interest to locations with statistically significant spatial and temporal clustering of high SST values. These areas also represent zones where seagrass can survive. Each correlation coefficient was determined for every month lag and the highest correlation coefficient determined the best time lag, indicating the length of the delayed response of the seagrass percent cover to the SST. After the best time lag was determined, the values of the seagrass cover was adjusted according to the number of months of its supposed delayed response to solidify further possible relationships of the increased SST, manifested by the determined hotspots, to the seagrass cover.

3. Results and Discussion

3.1 SST Profile of MOBPLS

Based on the DENR's 29.5°C baseline and 3°C thermal limit, satellite-derived SST data showed 28 instances above 32.5°C after the plant began operating in 1998, compared to only two in the six years prior. In the six years post-operation, there were seven such instances. While this suggests a potential impact from the plant, further investigation is needed to confirm causality.

3.1.1 Time Series Decomposition of SST: Figure 4 shows the decomposed SST time series into seasonal, trend, and remainder components. The seasonal part reflects natural cyclical fluctuations, while the remainder captures irregularities likely from sensor changes or environmental events. The trend component, the study's main focus, shows a steady SST increase from 1993 to 2023 across the shallow areas of the MOBPLS.

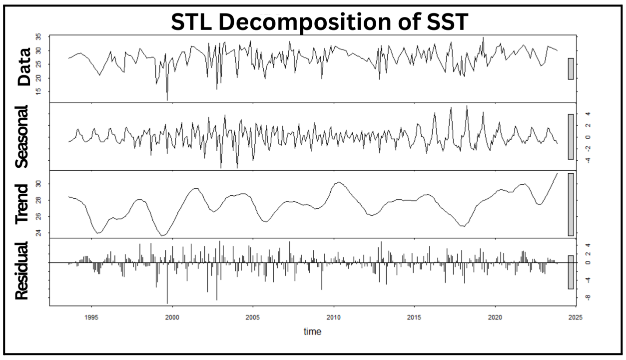

Figure 4. STL decomposition of SST in MOBPLS from 1993 to 2023. The *Data* panel shows the raw SST values, while the *Seasonal*, *Trend*, and *Residual* panels represent the corresponding decomposed time series components

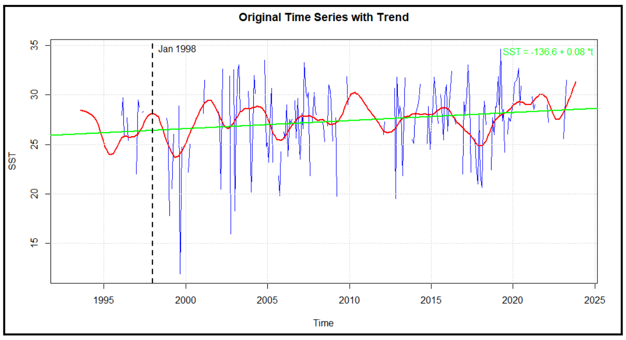

Figure 5. Overlay of the original time series and its decomposed trend component in MOBPLS from 1993 to 2023.

Meanwhile, Figure 5 displays the decomposed trend component overlaid on the original time series. Also shown is a linear trend line with a positive slope, which reinforces the observed increasing temperature trend over the years. The graph additionally marks the commencement of the plant's operation in 1998. While no specific month was indicated in existing literature, this visualization assumes the plant began operations as early as January 1998 for consistency.

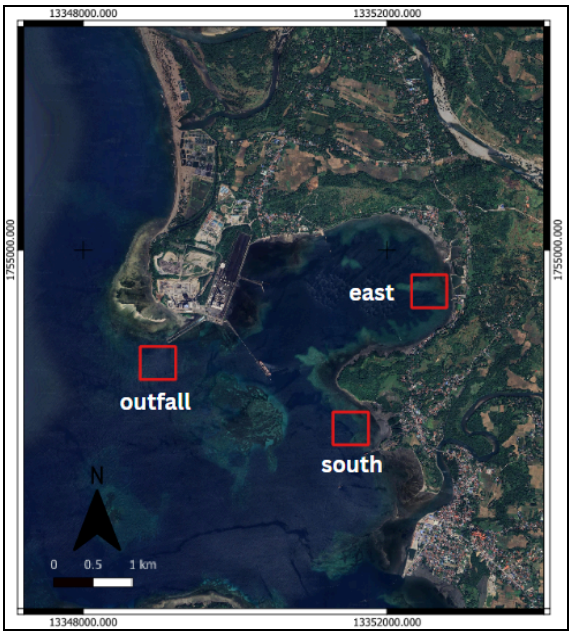

Figure 6. Location of the sites.

To better understand the behavior of SST in the area, a time series decomposition was conducted for SST values across several localized sites within the Masinloc-Oyon Bay Protected Landscape and Seascape. Specifically, the analysis focused on: (1) outfall: the area near the outfall, (2) east: a site within Oyon Bay that shares similar depth and bathymetric characteristics with the outfall, and (3) south: a site outside the bay to the south which also has a comparable profile. The exact locations of these areas are indicated in Figure 6. These locations were selected to assess whether elevated temperatures are consistent across these areas or if the outfall remains significantly warmer.

Figure 7 presents the trend components of SST in the selected locations. It is evident that SST values near the outfall are significantly higher than those in other locations, particularly after the power plant began operations in 1998. This suggests the significant influence of the power plant on the elevated temperature in its surrounding area.

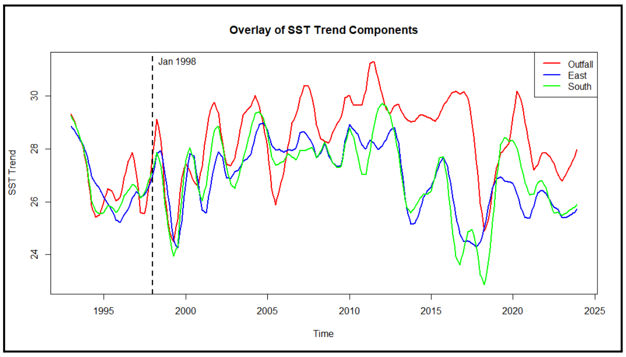

Figure 7. SST trend in the three selected locations

3.1.2 SST Hotspots: Figure 8 zooms into the power plant site on the peninsula west of Oyon Bay. In 1994, before the plant's operation, no significant SST patterns were observed. By 2003, five years post-operation, a cluster of elevated SST values appeared at the peninsula's tip, coinciding with the plant's outfall. This thermal plume persisted through 2023, indicating a long-term localized warming effect likely caused by the plant's discharge of heated effluent. The plume's extent illustrates the spatial reach of the thermal influence before the elevated temperatures dissipate into surrounding waters.

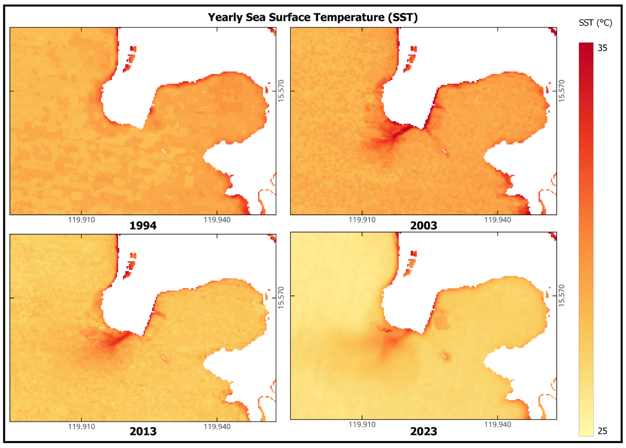

Figure 8. Zoomed in SST along the outfall of the plant pre-operation (1994) and SST along the outfall of the plant during the operational period (2003, 2013, 2023)

The SST hotspot map (Figure 9) reveals a progressively expanding hotspot at the plant's outfall, with 23 of the 26 operational years showing significant clustering which indicates an intensifying rise in SST directly in the discharge area. Along the coastlines of the study area, persistent hotspots were likewise detected. However, their clustering has remained relatively stable, suggesting that while these areas have consistently exhibited elevated temperatures since the start of the plant's operation, the trend has not intensified further. In contrast, sporadic hotspots surrounding the intensifying outfall region—defined as intermittent yet statistically significant—likely reflect the dispersal of heated effluent waters. This pattern supports the interpretation that thermal influence weakens gradually with distance from the outfall as it diffuses.

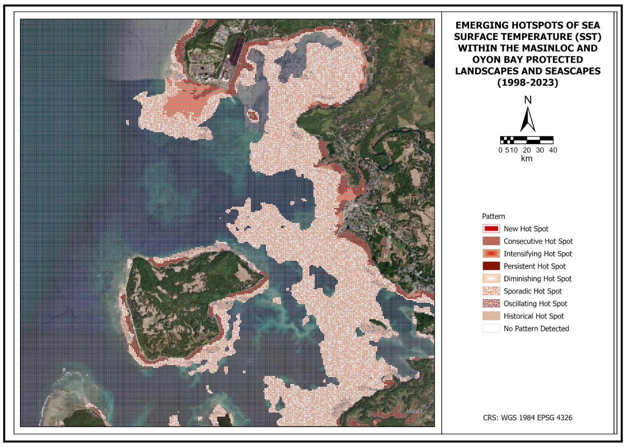

Figure 9. SST Hotspots based on the analysis of SST data from 1998 to 2023

3.1.3 SST Validation: As seen in Figure 10, although the values do not exactly match, the trends in land surface temperature (LST) and air temperature showed similar overall patterns. This difference in values is expected since LST and air temperature measure different aspects of temperature. The consistently higher LST values reflect the known difference due to the physical properties of the surfaces where heat is measured. Additionally, the trend line shows that LST increased at a faster rate than air temperature, which aligns with established findings (do Nascimento et al., 2022). Both data sets exhibited a general upward trend, supporting the reliability of the retrieval method when compared with observed temperature records. By extension, this also provides indirect validation for the SST values derived using the same single-channel technique.

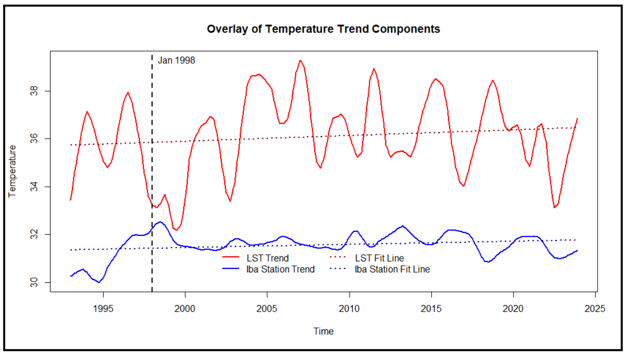

Figure 10. Satellite-derived LST and air temperature of PAGASA Iba, Zambales station

3.2 Seagrass Cover in the MOBPLS

Figure 11 shows the yearly seagrass percent cover in shallow water areas identified as intensifying and persistent SST hot spots. Before the power plant began operations, seagrass cover in the study area was about 50%. When the plant started in 1998, cover sharply declined to 27%, reaching a low of 17% in 2001. Between 2001 and 2006, the cover fluctuated but stabilized, indicating some adaptation resistance to thermal stress. From 2007 onward, seagrass cover increased to around 30% and remained fairly stable until 2023, peaking at 40% in 2010. Although it never returned to pre-operational levels, this pattern suggests partial adaptation despite ongoing exposure to heated effluent.

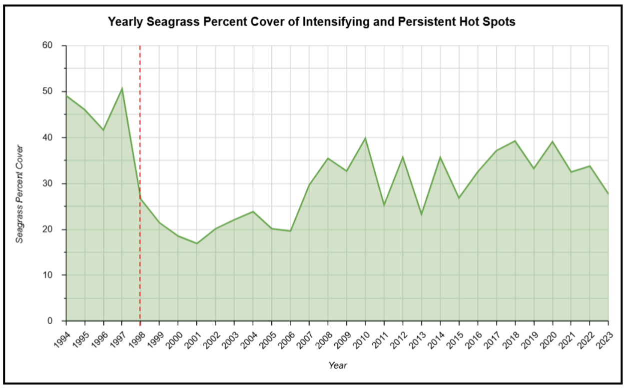

Figure 11. Yearly Seagrass Percent Cover in Intensifying and Persistent Hot Spot Areas. The red line marks the start of the power plant's operation.

This trend aligns with studies showing thermal stress reduces photosynthetic yield in seagrass species. The dominant species in the area, *Enhalus acoroides*, is relatively heat-tolerant, which may have enabled greater capacity for thermal acclimation, as suggested by the prolonged resistance phase and gradual recovery observed in this study.

3.2.1 Seagrass Validation: In 1999, seagrass classified by spectral unmixing covered about 3.85 km² at the 50% threshold, with 68.83% overlapping a reference map; at the 75% threshold, coverage increased to 7.98 km² with 72.31% overlap. For 2020, the 50% threshold yielded 8.47 km² with 66% overlap, while the 75% threshold showed 4.74 km² with 73% overlap. These overlaps support the spatial validity of the spectral unmixing method in detecting seagrass presence. Although precise accuracy assessment was not possible due to limited reference data, the consistent spatial agreement across years and thresholds suggests the method effectively identifies seagrass areas, making it suitable for temporal and ecological analysis.

3.3 Time-Lagged Correlation

3.3.1 Best Time Lag: Figure 12 shows the lagged correlation between the SST and seagrass percent cover within the study area across different time periods. The areas identified as intensifying and persistent hotspots were mostly located around the outfall of the plant and the shorelines of MOBPLS. Given that the seagrass percent cover had already increased by 2007 and had been stable until 2023, a different lagged correlation was obtained for 1998-2006 and 1998-2023 to account for the immediate and the long term effects, respectively. The period from 1998-2006 saw the highest correlation at R=-0.33 and had a seven-month lag, while the period from 1998-2023 had a six to seven-month lag as both time lags have a correlation coefficient of R=-0.19, the highest in the said period. The correlation coefficient indicates that the SST and seagrass percent cover are inversely proportional to each other and that there was a seven month delay in the response of the seagrass to the change in SST. Moreover, there was a higher correlation when considering the more recent period relative to the start of the plant's operations. Meanwhile in the areas identified as intensifying hot spots, which were mostly concentrated around the outfall of the plant, both periods had the highest correlation coefficient in the eight-month lag. The period from 1998 to 2006 had the highest correlation coefficient at R=-0.23, while the period from 1998-2023 had the highest correlation coefficient at R=-0.19. However, in this case, there was a lower correlation between the two variables and there was an eight-month delay in the response of the seagrass to the change in SST.

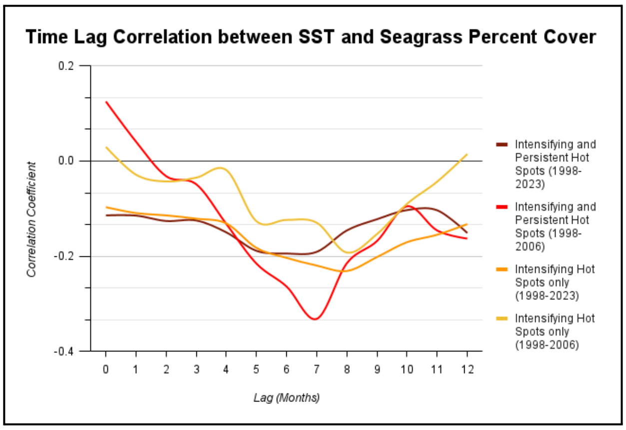

Figure 12. Time Lag Correlation between SST and seagrass percent cover

3.3.2 Relationship Between SST and Seagrass Cover: The computed correlation coefficient of the SST and the adjusted seagrass cover based on its 7-month delayed response was calculated to be at R=-0.47 (Figure 13). The negative correlation implied that as the SST increased, the seagrass cover consequently decreased.

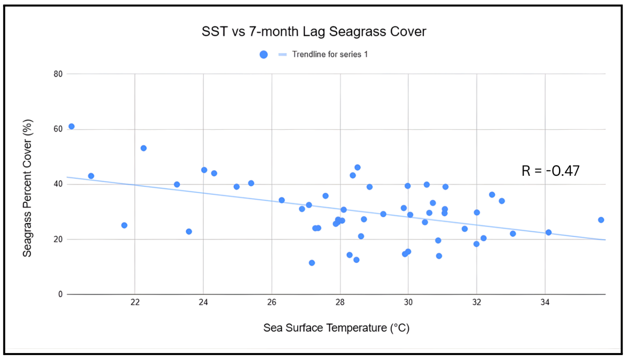

Figure 13. Scatter plot of the SST and the adjusted 7-month lagged seagrass cover

However, given the value of the correlation coefficient which was in between zero to 1, this implied a moderate negative correlation between the two variables. Hence, the SST does not necessarily have any correlation with the seagrass cover. Furthermore, the computed R² value of 0.22 indicates a weak linear relationship between SST and seagrass percent cover in the current dataset. In the context of this study, this may imply that other factors may be playing a more significant role in influencing seagrass variability. The moderate correlation between the SST and the seagrass percent cover was expected as there are various factors that affect seagrass health and eventually, seagrass cover. In the study of Reyes et al. (2021), water quality, measured through parameters such as dissolved oxygen, salinity, turbidity, pH, and nutrient concentrations (phosphate and nitrate), was found to correlate with seagrass biomass, a key indicator of seagrass health. While temperature was only one of the factors considered in their analysis, the present study specifically focuses on the effect of elevated SST, attributed to heated effluents from the power plant, on seagrass cover. Hence, despite the moderate correlation, the influence of SST should not be discounted as it remains a significant factor in water quality, further affecting seagrass health and seagrass cover.

4. Conclusion

This study investigated the occurrence of thermal pollution in the Masinloc and Oyon Bay Protected Landscapes and Seascapes (MOBPLS) due to heated effluent discharged by the Masinloc Power Plant, and its correlation with changes in seagrass percent cover. SST data from shallow waters, where seagrass typically thrives, was analyzed through time series decomposition, revealing a gradual long-term increase in SST. To distinguish local thermal pollution from global climate change, spatiotemporal hotspot analysis was performed. Results showed intensifying hot spots near the plant's outfall, persistent hotspots in the coastal areas, and sporadic hotspots in surrounding waters, indicating localized thermal impacts. These patterns suggest that the SST increase is related to the power plant rather than solely to broader climate trends. Seagrass cover in areas with persistent and intensifying SST hotspots showed a sharp decline, dropping to half its pre-operational levels shortly after the plant began operations. While partial recovery was observed, it remained below original levels, suggesting limited resilience potentially linked to thermal stress but not exclusively determined by it. Meanwhile, a time-lag correlation analysis revealed a weak negative correlation ($R=-0.33$) between SST and seagrass cover, with the latter responding about seven months after the temperature rise. This delayed response underscores a potential indicative relationship between thermal stress and seagrass decline, though other environmental factors such as water quality and turbidity also influence seagrass health, highlighting a key limitation of this study. In addition to that limitation, the study is also constrained by the absence of long-term in situ SST and seagrass measurements. Air temperature data from PAGASA were used as a proxy for validation, which, while suitable for long-term consistency, is an indirect approach.

5. Recommendations

While the study provides valuable insights on the hot spots of SST values along the study area and its correlation to the seagrass percent cover through time, further research is needed to build on the findings and address the limitations of this study. Hydrodynamic modelling of the water system within the Masinloc and Oyon Bay Protected Landscapes and Seascapes (MOBPLS) can be done to better understand the dispersion of heated effluents from the power plant. Modelling currents and mixing patterns can reveal how thermal plumes spread spatially and temporally. Additionally, incorporating in situ temperature measurements would enable a more detailed analysis of localized anomalies. Moreover, other factors affecting seagrass health in the area can be further explored. Furthermore, modern technologies should be utilized by the Masinloc Power Plant to better treat the cooling water such that its effects to the environment where it is discharged would be minimized. Given that the MOBPLS is a protected area under the law, the protection of benthic habitats, including seagrass meadows should be of priority as the health of the marine ecosystems ensure a rich marine biodiversity, which further contributes to the livelihood of the nearby communities relying on fisheries and eco-tourism.

References

Bach, B., Dragicevic, P., Archambault, D., Hurter, C., & Carpendale, S., 2016. A descriptive framework for temporal data visualizations based on generalized space-time cubes. *Computer Graphics Forum*, 36(6), 36–61. doi.org/10.1111/cgf.12804

do Nascimento, A. C. L., Galvani, E., Gobo, J. P. A., & Wollmann, C. A., 2022. Comparison between Air Temperature and Land Surface Temperature for the City of São Paulo, Brazil. *Atmosphere,* 13(3), 491. doi.org/10.3390/atmos13030491

Department of Energy, 2024. Monthly Gross Generation in MWh (Separate Grid / Off-Grid) For 2023. 2023 Power Statistics

Hill, V. J., Zimmerman, R. C., Byron, D. A., & Heck, K. L., 2024. Mapping Seagrass Distribution and Abundance: Comparing Areal Cover and Biomass Estimates Between Space-Based and Airborne Imagery. *Remote Sensing*, 16(23), 4351. doi.org/10.3390/rs16234351

Jiang, W.-Y., Zhang, Y.-H., Liu, Y.-C., Li, W.-T., Xu, J.-G., & Zhang, P.-D., 2022. The effect of abrupt increase in water temperature on the survival and growth of eelgrass Zostera marina. *Aquatic Botany*, 183, 103572. doi.org/10.1016/j.aquabot.2022.103572

Jimenez-Munoz, J. C., Cristobal, J., Sobrino, J. A., Soria, G., Ninyerola, M., & Pons, X., 2009. Revision of the single-channel algorithm for land surface temperature retrieval from Landsat thermal-infrared data. *IEEE Transactions on Geoscience and Remote Sensing*, 47(1), 339–349. doi.org/10.1109/tgrs.2008.2007125

Macreadie, P., & Hardy, S., 2018. Response of seagrass 'blue carbon' stocks to increased water temperatures. *Diversity*, 10(4), 115. doi.org/10.3390/d10040115

Mishra, S., Ghosh, A., Rai, K., Jaiswal, B., Yadav, D. S., Agrawal, M., & Agrawal, S. B., 2021. Dimensions of climate change and its consequences on ecosystem functioning. *Global Climate Change*, 109–149. doi.org/10.1016/b978-0-12-822928-6.00003-4

Paz-Alberto, A. M., Pakaigue-Hechanova, M., & Sigua, G., 2015. Assessing diversity and phytoremediation potential of seagrass in tropical region. *International Journal of Plant, Animal, and Environmental Sciences*, 5(4), 24–35.

Reyes, A. G. B., Salmo, S. G., Vergara, Ma. C. S., & Blanco, A. C., 2021. Seagrass biomass and sediment carbon in conserved and disturbed seascape. *Ecological Research*, 37(1), 67–79. doi.org/10.1111/1440-1703.12272

Wang, M., Zhang, Z., Hu, T., & Liu, X., 2018. A practical single‐channel algorithm for land surface temperature retrieval: Application to Landsat series data. *Journal of Geophysical Research: Atmospheres*. doi.org/10.1029/2018jd029330

Zhang, B., Zhang, Y., Wang, Z., Ding, M., Liu, L., Li, L., ... & Zhang, H., 2021. Factors driving changes in vegetation in Mt. Qomolangma (Everest). *Remote Sensing*, 13(22), 4725. doi.org/10.3390/rs13224725